Article

Li$_2$ZrO$_3$-Coated Monocrystalline LiAl$_{0.06}$Mn$_{1.94}$O$_4$ Particles as Cathode Materials for Lithium-Ion Batteries

Chunliu Li [1,2,†], Banglei Zhao [3,†], Junfeng Yang [1,4,*], Linchao Zhang [1,*], Qianfeng Fang [1,2] and Xianping Wang [1,*]

[1] Key Laboratory of Materials Physics, Institute of Solid State Physics, HFIPS, Chinese Academy of Sciences, Hefei 230031, China; lcliu@southmn.com (C.L.); qffang@issp.ac.cn (Q.F.)
[2] Science Island Branch, Graduate School of University of Science and Technology of China, Hefei 230026, China
[3] School of Management Science and Engineering, Anhui University of Finance and Economics, Bengbu 233030, China; zbl1234@mail.ustc.edu.cn
[4] Lu'an Branch, Anhui Institute of Innovation for Industrial Technology, Lu'an 237100, China
* Correspondence: jfyang@issp.ac.cn (J.Y.); lczhang@issp.ac.cn (L.Z.); xpwang@issp.ac.cn (X.W.)
† These authors contributed equally to this work.

Abstract: Li$_2$ZrO$_3$-coated and Al-doped micro-sized monocrystalline LiMn$_2$O$_4$ powder is synthesized through solid-state reaction, and the electrochemical performance is investigated as cathode materials for lithium-ion batteries. It is found that Li$_2$ZrO$_3$-coated LiAl$_{0.06}$Mn$_{1.94}$O$_4$ delivers a discharge capacity of 110.90 mAhg^{-1} with 94% capacity retention after 200 cycles at room temperature and a discharge capacity of 104.4 mAhg^{-1} with a capacity retention of 87.8% after 100 cycles at 55 °C. Moreover, Li$_2$ZrO$_3$-coated LiAl$_{0.06}$Mn$_{1.94}$O$_4$ could retain 87.5% of its initial capacity at 5C rate. This superior cycling and rate performance can be greatly contributed to the synergistic effect of Al-doping and Li$_2$ZrO$_3$-coating.

Keywords: lithium zirconium oxide; lithium manganese oxide; monocrystallite; cathode materials; lithium-ion batteries

1. Introduction

Spinel LiMn$_2$O$_4$ (LMO) has been recognized as one of the promising cathode materials for the lithium-ion batteries due to the environmental compatibility, low cost, and high specific capacity [1–4]. However, the poor rate performance caused by the low Li$^+$ conductivity and the rapid capacity fading induced by the Jahn–Teller distortion have severely impeded its commercial applications [5–7].

Nanocrystallization has been proved to be an effective way to improve the electrochemical kinetics by decreasing the diffusion path of Li$^+$ and enlarging contact area between electrode and electrolyte [8,9]. Nevertheless, the enlarged specific surface area will inevitably increase the side reactions. Although the ion-doping technique could alter the electrochemical properties to some extent, the capacity decay still occurs due to the Mn ions dissolution, especially under high temperatures [10–13]. Alternatively, surface coating is often adopted to improve the cycling performance by inhibiting the side reactions between LMO and electrolyte [14,15]. Unfortunately, the coating strategy cannot improve the transport kinetics of Li$^+$. Therefore, the combination of ion-doping and coating should be considered to make full advantages.

Except for the side reactions, the nanocrystallization will lead to flawed crystallinity which is harmful for the Li$^+$ ion transport, however LMO has a unique three-dimensional tunnel structure in which the Li$^+$ could transfer through the 8a-16c-8a pathway [16]. Therefore, the monocrystal size should not be the determining factor to restrain the Li$^+$ transport. Moreover, the micron-sized monocrystalline LMO modified with ion-doping and surface coating may simultaneously decrease the contact area with electrolyte and improve the electrochemical performance.

In this work, we propose combined tactics to fabricate micro-sized monocrystalline $LiAl_{0.06}Mn_{1.94}O_4$ particles with Li_3BO_3 as sintering additive. The resultant Li_2ZrO_3-coated and Al-doped micro-sized monocrystalline $LiMn_2O_4$ powder was adopted as cathode materials for lithium-ion batteries, and their electrochemical performance was investigated in detail.

2. Materials and Methods

The Li_2ZrO_3-coated micro-sized monocrystalline $LiAl_{0.06}Mn_{1.94}O_4$ was prepared with solid-state sintering. First, Li_2CO_3 (Aldrich, St. Louis, MI, USA), Al_2O_3 (Aldrich) and Mn_3O_4 (EMD, Aldrich) were ball-milled with the molar ratio of Li:Al:Mn = 1.06:0.06:1.94. The excess Li_2CO_3 was used to compensate the lithium loss during heat treating. Then, the mixture was sintered at 450 °C for 5 h. After that, the pre-sintered mixture was ball-milled with Li_2CO_3, H_3BO_3, and ZrO_2. Then, the mixture was sintered at 780 °C for 18 h. Li_3BO_3 and Li_2ZrO_3 could be synthesized as the following Equations (1) and (2).

$$H_3BO_3 + Li_2CO_3 \rightarrow Li_3BO_3 \qquad (1)$$

$$ZrO_2 + Li_2CO_3 \rightarrow Li_2ZrO_3 \qquad (2)$$
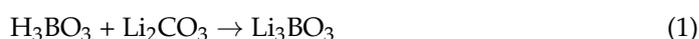
The detailed ingredient of the micron-sized monocrystalline $LiAl_{0.06}Mn_{1.94}O_4$ was listed in Table 1. As a comparison, the $LiMn_2O_4$ samples without Al-doping, Li_3BO_3 additive or Li_2ZrO_3-coating were also prepared through the same sintering process.

Table 1. Specific component of the micron-sized monocrystalline $LiMn_2O_4$ samples (* No addition).

Samples	Composition		
	$LiMn_2O_4$	Li_3BO_3	Li_2ZrO_3
LMO	$LiMn_2O_4$	*	*
LMO-B	$LiMn_2O_4$	1 mol%	*
LAMO-B	$Li Al_{0.06}Mn_{1.94}O_4$	1 mol%	*
LAMO-B-Zr1	$Li Al_{0.06}Mn_{1.94}O_4$	1 mol%	1 mol%
LAMO-B-Zr2	$Li Al_{0.06}Mn_{1.94}O_4$	1 mol%	2 mol%
LAMO-B-Zr3	$Li Al_{0.06}Mn_{1.94}O_4$	1 mol%	3 mol%
LAMO-B-Zr4	$Li Al_{0.06}Mn_{1.94}O_4$	1 mol%	4 mol%

Structural characterization of the samples was analyzed by X-ray diffraction (XRD, Rigaku SmartLab diffractometer) with Cu Kα radiation in the 2θ range of 10–70°. The particle size, surface morphology, and elemental composition were observed by scanning electron microscopy (SEM, Hitachi S-3400N) equipped with an energy dispersive spectrometer (EDS, Oxford 7426). The microstructure was detected with transmission electron microscopy (TEM, FEI Tecnai G2 F20). The samples were smashed before the TEM analysis.

Synthesized $LiMn_2O_4$ particle was mixed with carbon black and polyvinylidene fluoride (PVDF) with the mass ratio of 90:5:5 in N-methyl pyrrolidinone (NMP). Then, the slurry was coated on the aluminum foil and vacuum-dried at 100 °C. The electrode laminate was roll-pressed and punched to be discs with a diameter of 14 mm. The loading density of active material is approximately 5–8 mg cm^{-2}. The electrolyte was 1 M $LiPF_6$ in dimethyl carbonate (DMC)/ethyl carbonate (EMC)/ethylene carbonate (EC) (1:1:1, $v/v/v$). The 2032-type coin cells using Li metal as anode were prepared in an argon-filled glove box and tested in the voltage range of 3.0–4.3 V at several rates (1C = 148 mAhg^{-1}) on a battery test system (Neware). The cells were charged/discharged at 0.2C for 3 times first and then cycled at 0.5C for 200 times at 25 °C. Meanwhile, same cells were charged/discharged at 0.2C for 3 times and at 0.5C for 100 times at 55 °C, successively. Moreover, to evaluate the

rate performance, the cells were also charged at 0.5C and discharged at 0.5C, 1C, 2C, 3C, and 5C, respectively.

The electrochemical impedance spectroscopy (EIS) of the cells was performed on electrochemical workstation (CHI600E) with the frequency range of 10^5 to 10^{-2} Hz. The EIS tests were performed after the 1st and 200th cycle, respectively.

3. Results and Discussion

3.1. Li_3BO_3 Additive Promote the Grain Growth

The XRD patterns of the samples are shown in Figure S1. All the diffraction peaks match well with $LiMn_2O_4$ (JCPDF 35-0782). It proves that the Al-doping Li_3BO_3 additive or the Li_2ZrO_3-coating has no effect on the spinel cubic structure with the spatial group Fd3m. While focusing on the effect of the Li_3BO_3 additive, it could be found that the full width at half maximum (FWHM) of the LMO-B is much broader than that of the LMO (Table S1). As shown in Figure 1a, the FWHM of the main peaks of LMO are 0.188 (111), 0.152 (311), 0.155 (222), 0.163 (400), 0.151 (331), and 0.176 (511), respectively. While the corresponding values for the LMO-B are 0.071, 0.061, 0.053, 0.064, 0.066, and 0.073, respectively. It is suggested that the grain size of the monocrystal $LiMn_2O_4$ has grown up with the help of the Li_3BO_3 additive. Meanwhile, the conclusion is verified by the morphological observation (Figure 1b,c). The grain size of the LMO is less than 2 μm, while that of the LMO-B sample is approximately 2–8 μm according to the particle size distribution analysis (Figure S2). Both the XRD and SEM results prove that the Li_3BO_3 additive could promote the grain growth of monocrystal $LiMn_2O_4$ effectively.
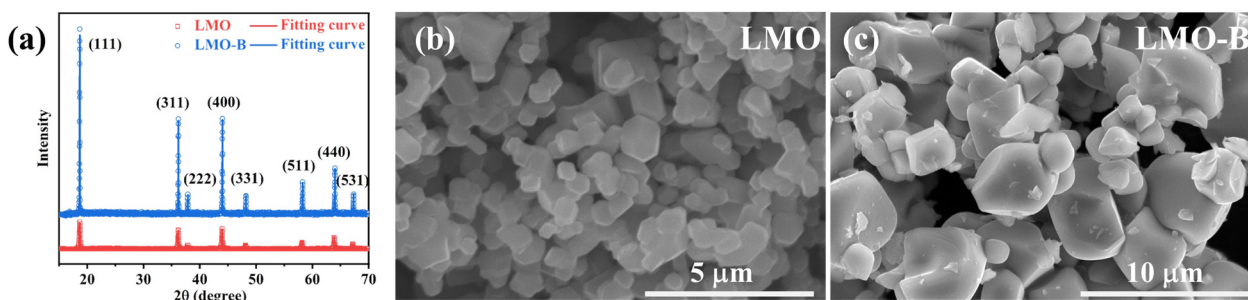

Figure 1. (**a**) XRD patterns of the LMO and LMO-B samples; the SEM images of the (**b**) LMO and (**c**) LMO-B.

3.2. Effect of the Al-Doping

With the Al-doping in $LiMn_2O_4$, the morphology of the LAMO-B (Figure 2a) has no significate change in comparison with the LMO-B sample (Figure 1c). While the systematic right shift of diffraction peaks could be observed, compared with the LMO-B sample, the main diffraction peaks of the LAMO-B sample shifted toward to the high angles as shown in Figure 2b. Meanwhile, the calculated lattice parameter of the LMO-B and LAMO-B is 8.2235 and 8.2090, respectively. It means that the Al atom with smaller radius has occupied the Mn site in the monocrystal $LiMn_2O_4$ lattice structure.

3.3. Li_2ZrO_3-Coating on the Monocrystal $LiMn_2O_4$

To analyze the influence of the Li_2ZrO_3-coating amount, the morphologies of the four samples with Al-doping and Li_2ZrO_3 coating were compared as shown in Figure 3. It is found that the micro-sized large grains are surrounded by smaller ones in all four samples and all the secondary particles show a diameter as large as ~10 mm. It proves that the Li_2ZrO_3 coating could not affect the size distribution.

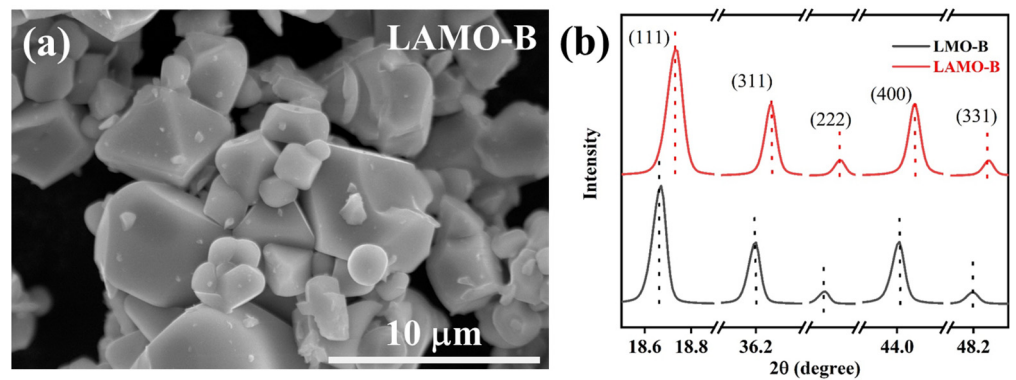**Figure 2.** (**a**) Morphology of the LAMO-B sample. (**b**) The comparison of diffraction peaks of LMO-B and LAMO-B samples.
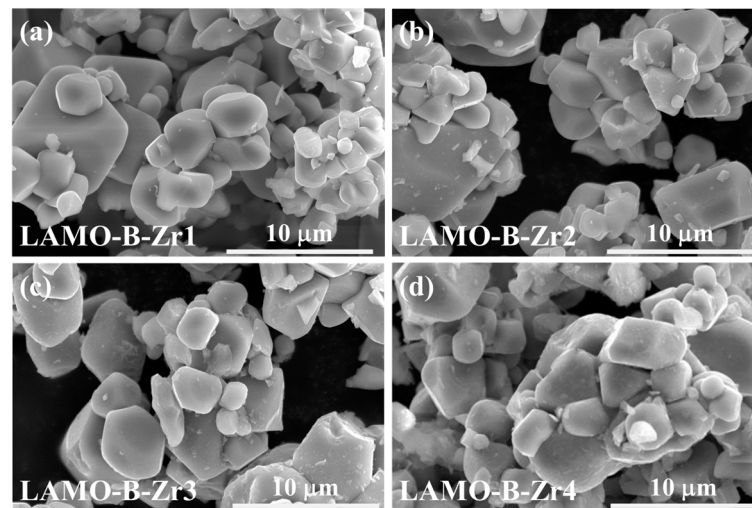

Figure 3. The SEM images of the (**a**) LAMO-B-Zr1; (**b**) LAMO-B-Zr2; (**c**) LAMO-B-Zr3 and (**d**) LAMO-B-Zr4 samples.

Meanwhile, it is found that the Al-doping and Li_2ZrO_3 coating distribute uniformly in the final samples. Taking the LAMO-B-Zr2 sample for example, the EDS mapping results exhibit uniform distribution of the Mn, Al, and Zr elements in the secondary particles as shown in Figure 4.
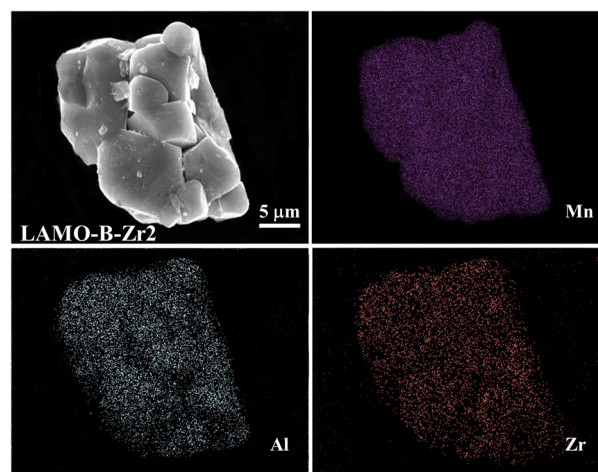

Figure 4. The EDS mapping of the LAMO-B-Zr2 sample.

To further observe the microstructure of the samples, TEM analysis and corresponding selected area electron diffraction (SAED) of the LMO-B are shown in Figure 5a. The diffraction spots can be indexed to (220), (111), (311), and (400) planes of cubic spinel $LiMn_2O_4$ (JCPDS 35-0782). Compared with the pristine surface of the LMO-B sample, a coating layer with a thickness of ~5.2 nm could be found in the LAMO-B-Zr2 sample (Figure 5b). Moreover, the coating layer should be brought from the Li_2ZrO_3 additive.
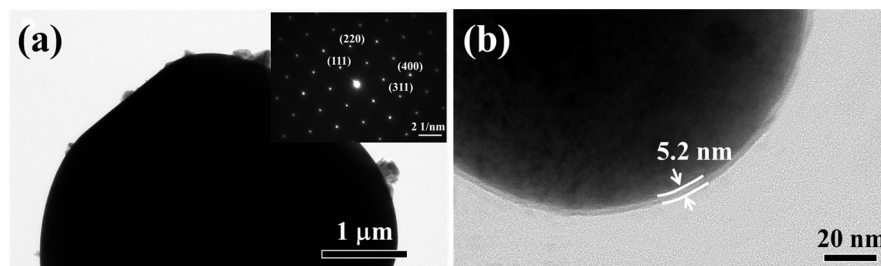

Figure 5. The TEM images and corresponding selected area electron diffraction (SAED) of the (**a**) LMO-B and (**b**) LAMO-B-Zr2.

3.4. Electrochemical Performances

The cycling and rating performance of the cells with the Al-doping and Li_2ZrO_3-coating samples was tested at the same conditions (Figure 6). The initial discharge capacity of the cells at 25 °C and 0.2C rate decreased steadily with the increscent Li_2ZrO_3-coating as shown in Figure 6a. It is reasonable, as the Li_2ZrO_3 provides no capacity contribution, the more coating, the less proportion of the active materials in the cell. Nevertheless, Li_2ZrO_3 aimed at reducing the side reactions serving as a protect layer. The effect of the Li_2ZrO_3-coating amount on the cycling performance at 25 °C and 55 °C is shown in Figure 6b,c, respectively. It was found that the capacity retention of the four samples is 93.0%, 93.9%, 90.2%, and 82.3% at 25 °C after 200 cycles with the increasing Li_2ZrO_3-coating amount. Moreover, at 55 °C, the corresponding capacity retention is 81.0%, 87.5%, 79.2%, and 79.5%, respectively. It is obvious that the LAMO-B-Zr2 could decrease the capacity loss and provide the optimal protection at both temperatures. Moreover, as shown in Figure 6d, the rate performance of LAMO-B-Zr2 is also better than the other three samples, especially at higher rates. Although the discharge capacity of LAMO-B-Zr2 at 0.5C is less than the LAMO-B-Zr1, the capacity at 1, 2, 3, and 5C rates is larger than the other three samples. It proves that the deficiency of Li_2ZrO_3 could not provide overall protection from the side reactions, while the excess of Li_2ZrO_3 would impede the migration of lithium ion. LAMO-B-Zr2 exhibited the best performance in a series of Al-doping and Li_2ZrO_3 coating samples.

To explore the influence of the Al-doping and the Li_2ZrO_3 coating, the electrochemical performance of the LMO-B, LAMO-B, and LAMO-B-Zr2 samples were characterized in parallel. Figure 7a presents the first charge–discharge curves obtained at 0.2C and 25 °C between 3.0 and 4.3 V (vs. Li/Li+). There are two voltage plateaus near 4.0 V and 4.1 V, which indicates the two-stage processes of Li+ ion insertion/extraction reactions for a typical characterization of a well-crystallized spinel $LiMn_2O_4$ [17,18]. The initial discharge specific capacities of the as-prepared samples show a decline trend with the Al-doping and the Li_2ZrO_3 coating. This result is comprehensible because the percentage of Mn^{3+} is partially occupied by the Al-doping or lowered by the Li_2ZrO_3 coating.
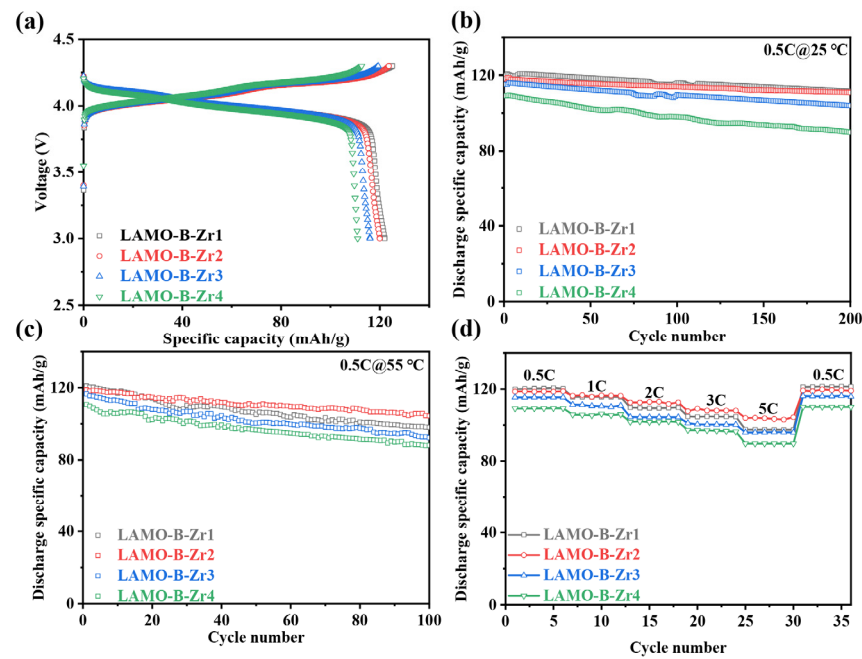
Figure 6. The electrochemical performance of the Li$_2$ZrO$_3$-coated LAMO-B-Zr cells. (**a**) The initial charge–discharge profiles at 0.2C and 25 °C; The cycling performance with 0.5C rate at (**b**) 25 °C and (**c**) 55 °C. (**d**) The rate performance at 0.5C, 1C, 2C, 3C and 5C, respectively.
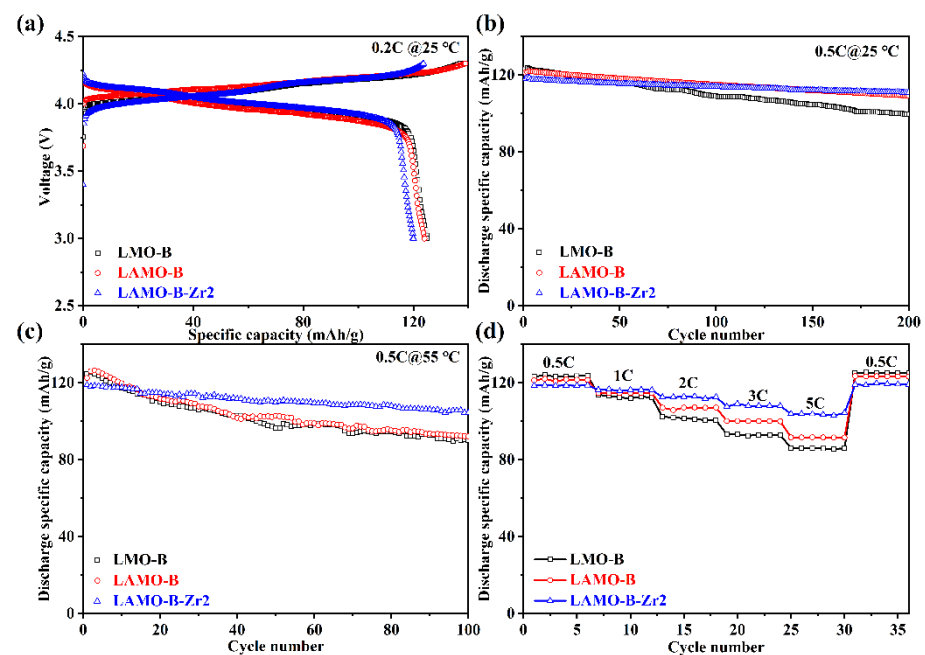

Figure 7. The electrochemical performance of the LMO-B, LAMO-B, and LAMO-B-Zr2 cells. (**a**) The initial charge-discharge profiles at 0.2 °C and 25 °C. The cycling stability with 0.5C rate at (**b**) 25 °C and (**c**) 55 °C. (**d**) The rate performance at 0.5C, 1C, 2C, 3C, and 5C, respectively.

However, according to the cycling stability at room temperature and 55 °C shown in Figure 7b,c, respectively, the capacity retention of the LAMO-B-Zr2 is much higher than that of the LMO-B and LAMO-B (Table 2). The possible reason may lie in that the Al-doping could stable the crystal structure during the cycling. Analogous results could be found in other literature reports [19,20]. On the other hand, with the help of the Li$_2$ZrO$_3$ coating, the capacity retention rate of the LAMO-B-Zr2 could go further to 93.9% after 200 cycles

at 25 °C and keep at 87.8% after 100 cycles at 55 °C. It turns out that the Li_2ZrO_3-coating could suppress the side-reactions effectively.

Table 2. The capacity retention ratios of LMO-B, LAMO-B, and LAMO-B-Zr2.

Samples	Capacity Retention Ratios	
	After 200 Cycles at 25 °C	After 100 Cycles at 55 °C
LMO-B	81.0%	72.2%
LAMO-B	90.0%	75.2%
LAMO-B-Zr2	93.9%	87.8%

Otherwise, the rate performance of the cells between 3.0 and 4.3 V (vs. Li/Li^+) is shown in Figure 7d. All the cells exhibit reduced discharge capacities as the increased C-rates. Although the capacity of LAMO-B-Zr2 at 0.5C is inferior to the other cells as the lowered proportion of active substances, the discharge capacities themselves or the capacity retention of the LAMO-B-Zr2 at 1C, 2C, 3C, and 5C rates are much higher than the other control samples. Moreover, the discharge capacity of LAMO-B-Zr2 could reach up to 103.41 $mAhg^{-1}$ at 5C.

The specific discharge capacity and the capacity retention of the LAMO-B-Zr2 sample at both room temperature and 55 °C are better than those of some reported $LiMn_2O_4$ single-crystalline and Al-doped $LiMn_2O_4$. The detailed comparisons of the electrochemical performance are listed in Table S2.

Furthermore, the EIS results of the LMO-B, LAMO-B, and LAMO-B-Zr2 cells after the 1st and 200th cycle is shown in Figure 8a,b, respectively. All the cells are discharged to 4.0 V before testing. All the Nyquist plots comprises two depressed semicircles in the high and middle frequency region and a straight line in the low frequency region. The intersection at the high frequency shows the Ohmic resistance (R_o), the diameter of the semicircle at the high frequency means the resistance (R_s) of solid electrolyte interface (SEI), and the diameter of the semicircle at low frequency suggests the resistance of the charge transfer (R_{ct}). The right intersection of the semicircle with the horizontal axis in the low frequency represent the total internal resistance ($R_t = R_o + R_s + R_{ct}$) [21,22]. The EIS plots were fitted with equivalent circuit shown in Figure 8a by Zview software. Moreover, the corresponding fitting results of the impedance are listed in Table 3. It is found that the Al-doping could decrease the impedance compared with the pristine LMO-B and the LAMO-B samples. It is suggested that the coating strategy is an efficient method of decreasing impedance.
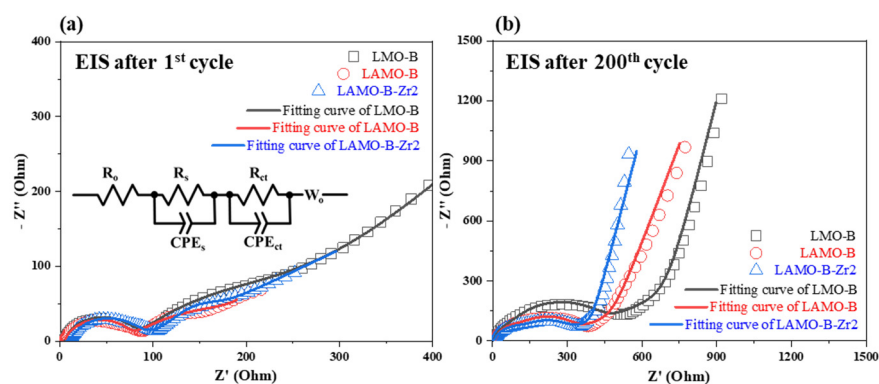

Figure 8. The Nyquist plots of the LMO-B, LAMO-B, and LAMO-B-Zr2 cells after the (**a**) 1st and (**b**) 200th cycle over the frequency range of 10^5 to 10^{-2} Hz. Inset figure is the equivalent circuit.

Table 3. The fitting results of the LMO-B, LAMO-B, and LAMO-B-Zr2 cells after the 1st and 200th cycle.

Sample	Rt (Ω) after 1st Cycle	Rt (Ω) after 200th Cycle
LMO-B	248.1	377.8
LAMO-B	235.8	293.1
LAMO-B-Zr2	101.1	270.8

4. Conclusions

The micron-sized monocrystalline $LiAl_{0.06}Mn_{1.94}O_4$ with a grain size of 2–8 μm was prepared in this work. With the synergistic modification of Al-doping and Li_2ZrO_3 coating, the cycling stability and rating performance have been significantly improved. Meanwhile, the optimal Li_2ZrO_3 coating amount was investigated. The LAMO-B-Zr2 with 2 mol% Li_2ZrO_3 addition possesses capacity retention of 93.9% after 200 cycles at room temperature and 87.8% after 100 cycles at 55 °C. This work provides appreciable point of view into the practical application of the LMO cathode in lithium-ion batteries.

Supplementary Materials: The following are available online at https://www.mdpi.com/article/10.3390/nano11123223/s1, Figure S1: The XRD patterns of the $LiMn_2O_4$ samples; Figure S2. The particle size distribution of the (**a**) LMO; (**b**) LMO-B; (**c**) LAMO-B-Zr1; (**d**) LA-MO-B-Zr2; (**e**) LAMO-B-Zr3; (**f**) LAMO-B-Zr4; Table S1: The full width at half maximum (FWHM) of the LMO and LMO-B samples; Table S2: Comparison of electrochemical performance of different $LiMn_2O_4$ electrode materials.

References

1. Paulsen, J.M.; Thomas, C.L.; Dahn, J.R. Layered Li-Mn-Oxide with the O2 Structure: A Cathode Material for Li-Ion Cells Which Does Not Convert to Spinel. *J. Electrochem. Soc.* **1999**, *146*, 3560–3565. [CrossRef]
2. Potapenko, A.V.; Kirillov, S.A. Enhancing high-rate electrochemical properties of $LiMn_2O_4$ in a $LiMn_2O_4/LiNi_{0.5}Mn_{1.5}O_4$ core/shell composite. *Electrochim. Acta* **2017**, *258*, 9–16. [CrossRef]
3. Kim, J.-S.; Kim, K.; Cho, W.; Shin, W.H.; Kanno, R.; Choi, J.W. A Truncated Manganese Spinel Cathode for Excellent Power and Lifetime in Lithium-Ion Batteries. *Nano Lett.* **2012**, *12*, 6358–6365. [CrossRef]
4. Tarascon, J.M.; Armand, M. Issues and challenges facing rechargeable lithium batteries. *Nature* **2001**, *414*, 359–367. [CrossRef] [PubMed]
5. Armand, M.; Tarascon, J.M. Building better batteries. *Nature* **2008**, *451*, 652. [CrossRef] [PubMed]
6. Michalska, M.; Ziółkowska, D.A.; Jasiński, J.B.; Lee, P.H.; Ławniczak, P.; Andrzejewski, B.; Ostrowski, A.; Bednarski, W.; Wu, S.H.; Lin, J.Y. Improved electrochemical performance of $LiMn_2O_4$ cathode material by Ce doping. *Electrochim. Acta* **2018**, *276*, 37–46. [CrossRef]

7.　Jiang, C.; Tang, Z.; Wang, S.; Zhang, Z. A truncated octahedral spinel $LiMn_2O_4$ as high-performance cathode material for ultrafast and long-life lithium-ion batteries. *J. Power Source* **2017**, *357*, 144–148. [CrossRef]

8.　Zhu, X.; Wu, X.; Doan, T.N.L.; Tian, Y.; Zhao, H.; Chen, P. Binder-free flexible $LiMn_2O_4$/carbon nanotube network as high power cathode for rechargeable hybrid aqueous battery. *J. Power Source* **2016**, *326*, 498–504. [CrossRef]

9.　Cao, J.; Guo, S.; Yan, R.; Zhang, C.; Guo, J.; Zheng, P. Carbon-coated single-crystalline $LiMn_2O_4$ nanowires synthesized by high-temperature solid-state reaction with high capacity for Li-ion battery. *J. Alloys Compd.* **2018**, *741*, 1–6. [CrossRef]

10.　Yi, T.-F.; Xie, Y.; Wu, Q.; Liu, H.; Jiang, L.; Ye, M.; Zhu, R. High rate cycling performance of lanthanum-modified $Li_4Ti_5O_{12}$ anode materials for lithium-ion batteries. *J. Power Source* **2012**, *214*, 220–226. [CrossRef]

11.　Chen, M.; Chen, P.; Yang, F.; Song, H.; Liao, S. Ni, Mo Co-doped Lithium Manganate with Significantly Enhanced Discharge Capacity and Cycling Stability. *Electrochim. Acta* **2016**, *206*, 356–365. [CrossRef]

12.　Fu, Y.; Jiang, H.; Hu, Y.; Dai, Y.; Zhang, L.; Li, C. Synergistic Enhancement Effect of Al Doping and Highly Active Facets of $LiMn_2O_4$ Cathode Materials for Lithium-Ion Batteries. *Ind. Eng. Chem. Res.* **2015**, *54*, 3800–3805. [CrossRef]

13.　Wang, J.; Zhang, Q.; Li, X.; Wang, Z.; Guo, H.; Xu, D.; Zhang, K. Sputtering graphite coating to improve the elevated-temperature cycling ability of the $LiMn_2O_4$ electrode. *Phys. Chem. Chem. Phys.* **2014**, *16*, 16021–16029. [CrossRef]

14.　Tron, A.; Park, Y.D.; Mun, J. AlF_3-coated $LiMn_2O_4$ as cathode material for aqueous rechargeable lithium battery with improved cycling stability. *J. Power Source* **2016**, *325*, 360–364. [CrossRef]

15.　Waller, G.H.; Brooke, P.D.; Rainwater, B.H.; Lai, S.Y.; Hu, R.; Ding, Y.; Alamgir, F.M.; Sandhage, K.H.; Liu, M.L. Structure and surface chemistry of Al_2O_3 coated $LiMn_2O_4$ nanostructured electrodes with improved lifetime. *J. Power Source* **2016**, *306*, 162–170. [CrossRef]

16.　Wang, L.; Wu, B.; Mu, D.; Liu, X.; Peng, Y.; Xu, H.; Liu, Q.; Gai, L.; Wu, F. Compounds, Single-crystal $LiNi_{0.6}Co_{0.2}Mn_{0.2}O_2$ as high performance cathode materials for Li-ion batteries. *J. Alloys Compd.* **2016**, *674*, 360–367. [CrossRef]

17.　Li, J.; Cameron, A.R.; Li, H.; Glazier, S.; Xiong, D.; Chatzidakis, M.; Allen, J.; Botton, G.; Dahn, J. Comparison of single crystal and polycrystalline $LiNi_{0.5}Mn_{0.3}Co_{0.2}O_2$ positive electrode materials for high voltage Li-ion cells. *J. Electrochem. Soc.* **2017**, *164*, A1534. [CrossRef]

18.　Jiang, Q.; Liu, D.; Zhang, H.; Wang, S. Plasma-Assisted Sulfur Doping of $LiMn_2O_4$ for High-Performance Lithium-Ion Batteries. *J. Phys. Chem. C* **2015**, *119*, 28776–28782. [CrossRef]

19.　Liu, J.; Li, G.; Yu, Y.; Bai, H.; Shao, M.; Guo, J.; Su, C.; Liu, X.; Bai, W. Synthesis and electrochemical performance evaluations of polyhedra spinel $LiAl_xMn_{2-x}O_4$ (x≤0.20) cathode materials prepared by a solution combustion technique. *J. Alloys Compd.* **2017**, *728*, 1315–1328. [CrossRef]

20.　Taniguchi, I.; Song, D.; Wakihara, M. Electrochemical properties of $LiM_{1/6}Mn_{11/6}O_4$ (M = Mn, Co, Al and Ni) as cathode materials for Li-ion batteries prepared by ultrasonic spray pyrolysis method. *J. Power Source* **2002**, *109*, 333–339. [CrossRef]

21.　Yang, C.; Yu, S.; Lin, C.; Lv, F.; Wu, S.; Yang, Y.; Wang, W.; Zhu, Z.-Z.; Li, J.; Wang, N.; et al. $Cr_{0.5}Nb_{24.5}O_{62}$ Nanowires with High Electronic Conductivity for High-Rate and Long-Life Lithium-Ion Storage. *ACS Nano* **2017**, *11*, 4217–4224. [CrossRef] [PubMed]

22.　Tao, S.; Zhao, H.; Wu, C.; Xie, H.; Cui, P.; Xiang, T.; Chen, S.; Zhang, L.; Fang, Y.; Wang, Z.; et al. Enhanced electrochemical performance of MoO_3-coated $LiMn_2O_4$ cathode for rechargeable lithium-ion batteries. *J. Mater. Chem. A* **2017**, *199*, 203–208. [CrossRef]